Orientation Mapping of Graphene in a Scanning Electron Microscope*

Benjamin W. Caplins[a,*], Jason D. Holm[a], Robert R. Keller[a]

[a] *National Institute of Standards and Technology, Applied Chemicals and Materials Division, 325 Broadway, Boulder, CO, 80305, United States*

Abstract

A scanning transmission electron diffraction method is developed for use in the scanning electron microscope to perform orientational characterization of 2D materials. The method can generate orientation maps of monolayer graphene over a field of view up to $\approx 50\,\mu$m in just a few minutes and can distinguish twisted bilayers from aligned bilayers. This method holds promise to bring electron-diffraction-based orientation measurements of 2D materials to a broader audience.

1. Introduction

Two-dimensional (2D) materials have attracted significant attention for their extraordinary mechanical, thermal, and electronic properties.[1] Materials such as graphene and transition metal dichalcogenides have become some of the most intensely studied materials of the last decade. While many studies seek to characterize the properties of defect-free 2D materials, in real applications these materials will have defects which can significantly affect the remarkable properties. For example, grain boundaries can affect the thermal conductivity,[2, 3] electrical properties,[4, 5] and mechanical properties.[6, 7, 8] In multilayer systems, lattice twist angles can lead to emergent phenomenon such as superconductivity.[9] Thus, the ability to rapidly characterize the structure of 2D materials is not only critical for interpreting device behavior, but also for optimizing synthesis procedures and long-term device performance.

Crystallographic characterization of 2D materials can be divided into direct and indirect methods. Indirect methods seek to correlate atomic scale structure with phenomena that occur on larger length scales. Examples include observing the anisotropic epitaxial growth modes of adlayers,[10, 11] or probing the anisotropic optical properties of the material.[12, 13] Direct methods resolve the atomic structure in real or reciprocal space. Real space methods primarily include scanning probe techniques[14] and (scanning) transmission electron microscopy, [15, 16] but they are difficult to apply to large areas. Electron diffraction experiments resolve the atomic scale structure in reciprocal space and have been highly successful at characterizing the structure of 2D materials.[17, 18, 19, 20]

Particularly important for characterizing graphene has been dark-field transmission electron microscopy (DF-TEM).[17, 18] In DF-TEM an aperture is placed in the back focal plane of the objective lens to select electrons scattered with a particular wavevector. If the wavevector is selected to coincide with a particular reciprocal lattice vector of the sample, then the images formed will emphasize the areas of the sample with that particular (in-plane) orientation. By exhaustively selecting each graphene wavevector observed in the diffraction pattern, a stack of images can be constructed which can then be used to compute the lattice orientation of each pixel in the image. While this technique is powerful, it remains out of reach for many due to the relative inaccessibility of TEMs.

Hence, a more accessible crystallographic characterization method for 2D materials is desirable. Herein, we demonstrate a DF transmission imaging technique called ϕ-scan dark-field (ϕ-scan DF) microscopy that can easily be implemented in a conventional scanning electron microscope (SEM). As a DF imaging technique, it generates significant image contrast from extremely weakly scattering samples such as graphene even in the presence of unwanted contamination. The convergent beam of an SEM gives it an ultimate resolution limited only by the quality of the electron optics (on the order of 1 nm for most modern field emission SEMs), while also enabling the investigation of large fields of view. An added benefit of using an SEM relative to a TEM is that the lower energy electrons should not cause knock-on damage[21, 22] while also having a greater scattering cross section, which will improve signal strength. Herein, we apply this technique to a graphene sample as an example sample platform. We demonstrate how the method can be used to generate an orientation map and can distinguish twisted from aligned graphene bilayers.

*Corresponding Author

Email address: benjamin.caplins@nist.gov (Benjamin W. Caplins)

2. Methods and Results

A schematic of the technique is shown in Figure 1(a). An SEM (LEO Gemini 1525)[1] scans a 30 kV convergent electron probe across a nominally monolayer graphene sample supported on lacey carbon (Ted Pella, 21710). A small fraction of the incident probe (≈ 1 % as per a kinematic model[23]) diffracts off the graphene lattice (Figure 1(b)-(c)) as it transmits through the sample. The transmitted electrons are incident on a mask (Figure 1(d)), and the electrons selected by the mask are detected with a solid-state diode detector (KE Developments) forming an image as the electron probe is rastered across the sample.[24] During the course of a ϕ-scan DF experiment, the angle between the mask and the sample is stepped over the range 0° to 60° and 20-30 different dark-field images are collected. These images are then aligned using the SIFT method[25] in post-processing and form a datacube denoted, $I(x, y, \phi)$.

The mask was fabricated from household aluminum foil (12 μm thick) using a focused Ga^+ beam and is designed to select the 2nd order diffraction spots of graphene (see Figure 1(c)-(d)). When the angle ϕ (measured clockwise from the image horizontal to the first hole) equals ϕ_g (the in-plane crystallographic angle of the graphene lattice) the diffracted electrons will generate a bright area in an image. Here, ϕ is varied by compucentrically rotating the sample using the SEM sample stage, while holding the mask and detector fixed.[26] To simplify the interpretation, the image data is mapped into the rotating reference frame of the sample where the image horizontal is chosen to correspond to $\phi = 0°$. Thus for simplicity, the mask can be interpreted as moving while the sample remains stationary.

Most SEMs do not have a diffraction camera, so proper mask alignment is necessary and potentially non-intuitive. First, the camera length must be adjusted by translating the detector along the optic axis to permit the Bragg diffracted electrons to properly transmit the as-fabricated mask for the material under study. Next, the beam is focused at the sample plane (with the sample translated out of the way) and the detector is adjusted such that the mask is centered on the optic axis. Fine adjustments, if necessary, can be made with the electronic beam shift. This simple alignment procedure is sufficient in most cases to obtain observable diffraction contrast. Once diffraction contrast is visible, the mask position and camera length can be optimized to maximize the contrast at a grain boundary.

The ϕ-scan DF technique is demonstrated in Figure 2. Conventional imaging modes including secondary electron, bright-field transmission, and annular DF transmission (Figure 2(a)-(c)) of the graphene sample exhibit little contrast. Linear features are due to wrinkles[28] and

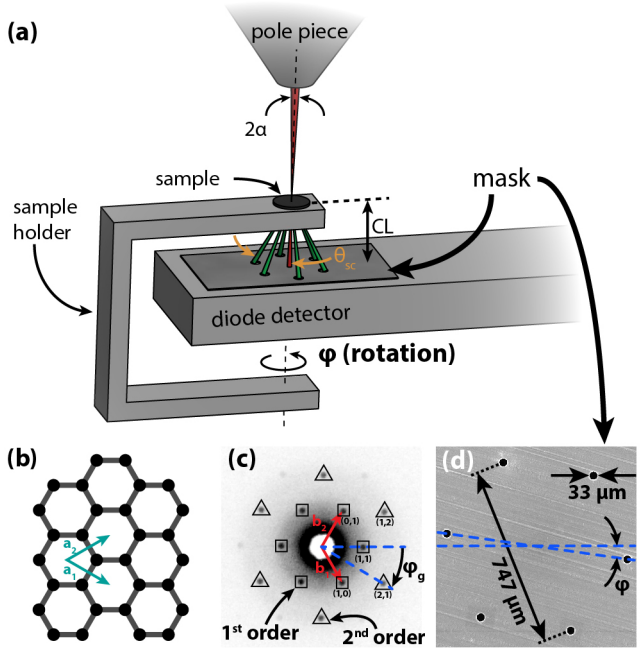

Figure 1: (a) A schematic of the measurement setup. The electron beam is focused on a graphene sample mounted on a c-shaped holder. A solid-state diode detector covered with a hexagonal mask is positioned beneath the sample. The camera length, $CL = 6.575$ mm, is selected such that the 2nd order spots (triangles) diffracted by the graphene lattice ($\theta_{scat} = 56.7$ mrad) can pass through the holes in the mask when $\phi = \phi_g$. (b) Graphene lattice in real space with lattice vectors shown. (c) Diffraction pattern collected on monolayer graphene using a 30 kV electron beam ($\alpha = 1.8$ mrad) using a recently reported imaging detector.[27] Reciprocal lattice vectors are shown. The angle ϕ_g characterizing the graphene lattice orientation is measured clockwise from the image horizontal. (d) A secondary electron image of the mask. The angle ϕ is experimentally controlled by rotating the sample and is referenced clockwise with respect to the image horizontal.

folds[29] in the graphene sheet, and small spots are due to debris on the surface. The remaining contrast is attributed to polymer residue that covers the sample.[30] In stark contrast to the conventional imaging modes, the three ϕ-scan DF images (Figure 2(d)-(f)) taken at $\phi = 0°$, $\phi = 36°$, and $\phi = 42°$ unambiguously segment the image into three distinct regions. To confirm the origin of this contrast, diffraction patterns were collected in the three regions (Figure 2(g)-(i)) using a recently reported imaging detector.[27] Each of the diffraction patterns is consistent with single domain graphene, but with each region having different in-plane orientations. A kinematic theory assuming normal beam incidence predicts intensity ratio of the 1st order diffraction spots to the 2nd order diffraction spots of $I_2/I_1 = 0.96$ for monolayer graphene and $I_2/I_1 = 3.6$ for AB stacked bilayer graphene.[23] The six-fold symmetry-averaged intensity ratio observed here was $I_2/I_1 = 1.0$, which strongly supports the assignment of the graphene to be monolayer thickness.[31, 32]

To more clearly understand how the diffraction pattern relates to the ϕ-scan DF dataset, the spatially averaged data for the three regions shown in Figure 2(a) is plot-

[1] Commercial instruments, equipment, or materials are identified only in order to adequately specify certain procedures. In no case does such an identification imply recommendation or endorsement by NIST, nor does it imply that the products identified are the best available for the purpose.

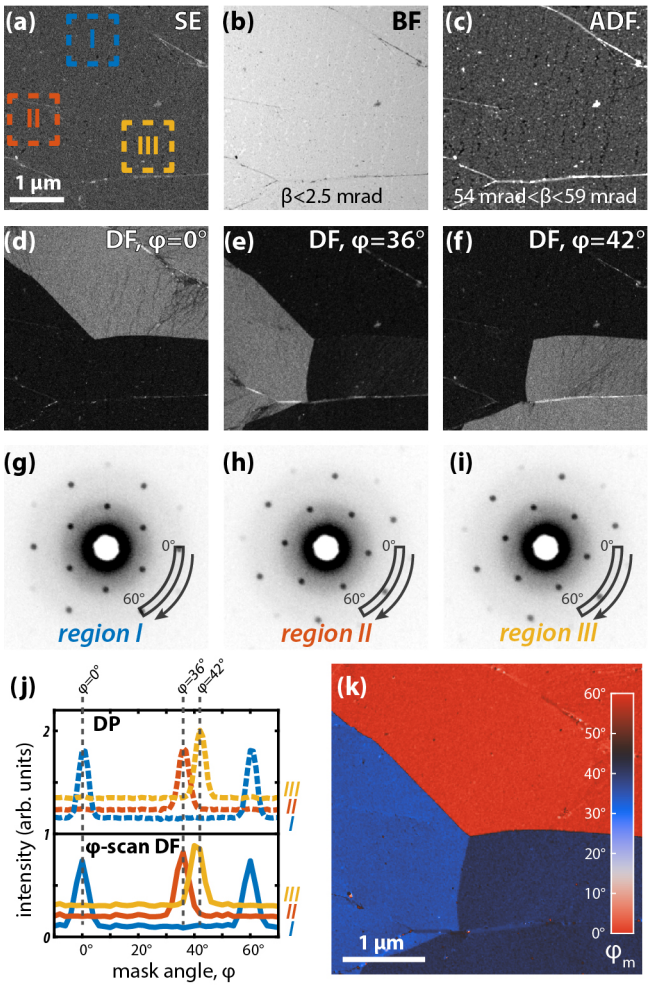

Figure 2: (a)-(f) Real space images of the same region of monolayer graphene recorded with different imaging conditions. (a)-(c) Conventional imaging conditions: secondary electron, bright-field, and annular dark-field. The relevant detector acceptance angle is given as β. (d)-(f) DF imaging conditions utilizing the hexagonal mask shown in Figure 1(d) at three different mask angles. (g)-(i) Diffraction patterns collected for the regions indicated in (a). (j) Solid lines are the observed DF intensity vs. ϕ for the spatial regions indicated in (a). Dashed lines are the analogous measurements except derived numerically from the annular sector of the diffraction patterns shown in (g)-(i). The ϕ values corresponding to images (d)-(f) are indicated by vertical dashed lines. (k) A colorized image of the same spatial region showing the orientation of the graphene lattice derived from the DF images. All data was collected with a beam convergence semiangle $\alpha = 1.8$ mrad.

ted in Figure 2(j). For the ϕ-scan DF data, the intensity vs. ϕ is plotted as solid lines and the analogous measurements obtained from the diffraction patterns are plotted as dashed lines. The three dark-field images (Figure 2(d)-(f)) correspond to the maximum in the ϕ-scan plots and yield an interpretation for the ϕ-scan DF data.

Although $I(x, y, \phi)$ contains the graphene lattice orientational information, the data have more than three channels and cannot be directly plotted for viewing. A data reduction must occur for display purposes. Since the sample is nominally monolayer graphene, the lattice orientation can be denoted with a single variable, ϕ_g. A computationally efficient method that can take the intensity vs. ϕ data at each pixel and output a continuous variable that approximates ϕ_g without resorting to nonlinear fitting methods for each pixel is desirable. The method used here is borrowed from directional statistics[33] and is given by:

$$\phi_m(x, y) = \frac{1}{6} \arg \left[\int_0^{2\pi} I(x, y, \phi)\, e^{-6i\phi} d\phi \right].$$

This method is a symmetry adapted calculation of the angular centroid of the ϕ-scan data and serves as a metric of the peak center. The application of this formula to the data is shown in Figure 2(k) using a circular color map and shows an obvious segmentation of the image into three grains with different orientation.

Images in an SEM are formed by rastering the beam across the sample. This, in turn, will cause the diffraction pattern to translate at the detector plane and will therefore not, in general, be centered on the optic axis. In other words, real space coordinates affect the wavevector selected by the mask. These translations require the field of view to be 'small' where the definition of 'small' depends on the type of measurement being performed. For the DF measurement being performed here, the convolution of the mask transmission function and the observed specimen diffraction pattern sets the relevant length scale. For example, data collected using a beam convergence an-

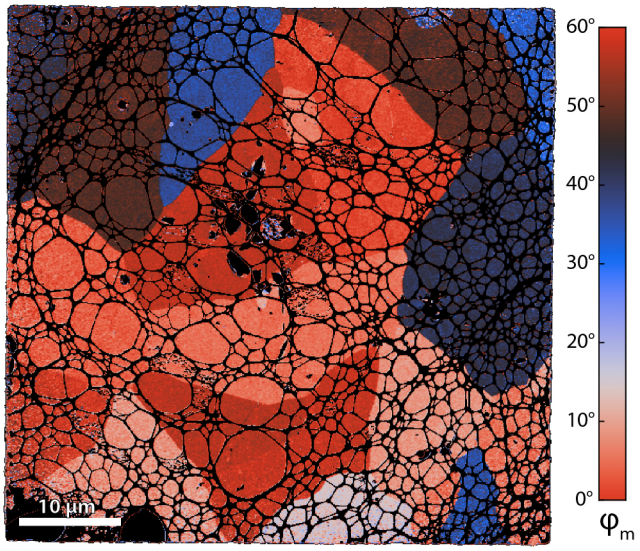

Figure 3: An orientation map of a full TEM grid square (ca. 53 μm wide) of nominally monolayer graphene. Regions corresponding to holes (vacuum), lacey carbon, or debris are identified via thresholding and are colored black. This map is derived from 20 ϕ-scan DF images collected in 3° steps at a resolution of 1024 × 768 (ca. 1 nA beam with a 5.3 mrad beam convergence semiangle). Total wall clock time for the collection of these 20 images was 496 s of which 206 s was spent actually scanning the sample with the electron beam; the remaining 290 seconds was spent moving and allowing for the stage to settle. A conservative estimate of the effective per-pixel data collection rate for the displayed data is 940 pixels/second.

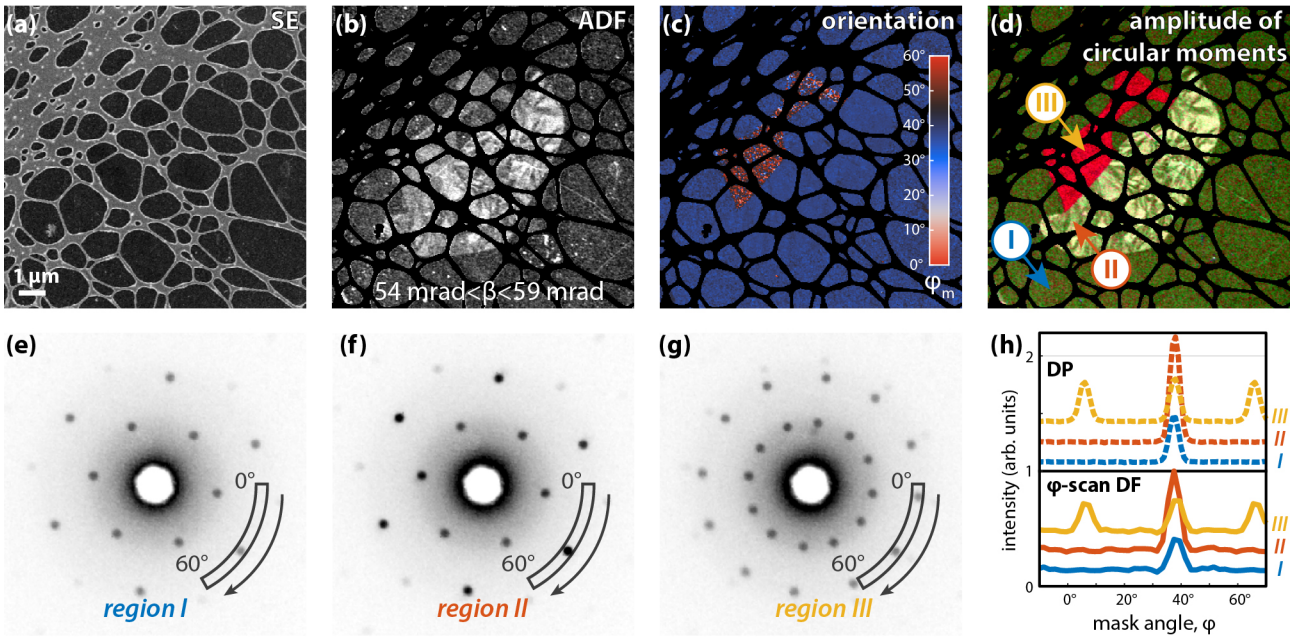

Figure 4: (a)-(d) Real space images of the same area of a graphene film exhibiting a bilayer region with two distinct orientations. (a) A secondary electron image. (b) Annular dark-field image. The lacey carbon is identified via a thresholding procedure and colored black. The detector acceptance angle, is given as β. (c) An orientation map using the same color bar as in Fig 3. Note that for multilayer regions with large twist angles, the orientation map can no longer directly indicate the orientation of the graphene lattice. (d) An image derived from the first three circular moments of the collected angular data that highlights the differences between monolayer regions and different bilayer regions (see text for details). (e)-(g) Diffraction patterns from the spatial regions identified in (d). (h) Solid lines are the observed dark-field intensity vs. ϕ for the spatial regions indicated in (d). Dashed lines are the analogous measurements except derived numerically from the annular sector of the diffraction patterns shown in (e)-(g).

gle $\alpha = 5.3$ mrad results in a bright field disc of $\approx 70\,\mu$m diameter at the mask plane enabling orientation mapping on this length scale. Figure 3 shows the orientation map over a full TEM grid square (53 μm field of view) of lacey carbon supported monolayer graphene. Note that for a field of view greater than the width of the bright field disc, the convolution of mask transmission function and specimen diffraction pattern can significantly bias the calculated ϕ_m values away from ϕ_g and care must be taken in the interpretation. Larger fields of view, however, can easily be obtained by stitching together multiple fields of view collected at different sample stage positions.

The angular resolution of the calculation of ϕ_m is primarily limited by the ability to calculate the center of the peak in intensity along the ϕ-axis (e.g. in Figure 2(j)). Thus, while larger beam limiting apertures will increase the total collected signal and also the maximum field of view attainable, it will also increase the width of the peak (with respect to the ϕ-axis) and thus have a deleterious effect on the ability to localize the peak. This, however, can be offset by improving the signal-to-noise with either an increased signal collection time or post-processing denoising. The balance between these effects will depend on the microscope being used, the sample being investigated, and the information that is desired. For the orientation map in Figure 3, the collection time is short (10.3 seconds of integration per dark-field image) and could be easily extended if necessary. For the data in Figure 3, the standard deviation of the ϕ_m values from a homogenous region of pixels is used as a measure of the measurement resolution and ranges from 1° at the center of the field of view to 3° at the extreme corners of the field of view.

This work demonstrates the ability of the ϕ-scan DF technique to map grain orientation of monolayer graphene films. In addition, it has the ability to lend insight into the structure of multilayer structures. Figures 4(a)-(d) show a region of graphene recorded with different imaging conditions. Except for lacey carbon support structures, the secondary electron image (Figure 4(a)) is relatively featureless. The annular DF image (Figure 4(b)), however, shows a bright region the middle of the image that can be attributed to multiple layers of graphene.[34] The corresponding ϕ_m map suggests the bright center region may have two distinct layer stackings. For a more descriptive visualization of the data, quantities proportional to the amplitude of the first three circular moments[33] are computed at each pixel:

$$A_n(x,y) = \left| \int_0^{2\pi} I(x,y,\phi)\, e^{-6ni\phi} d\phi \right| \quad n \in \{1,2,3\}\,.$$

Then a decorrelation stretch algorithm[35] is used to generate RGB values from the three calculated amplitudes. This color representation of the $I(x,y,\phi)$ data (Figure 4(d)) is sensitive to changes in the shape of the intensity vs. ϕ plots and suggests that the field of view contains three different regions denoted I, II, and III.

Diffraction patterns and intensity vs. ϕ plots for regions I, II, and III are shown in Figures 4(e)-(h). The ratio of the 1st and 2nd order diffraction spots show that region I contains monolayer graphene which appears to extend into all three regions. The diffraction pattern from region II is consistent with a bilayer where the second layer is roughly aligned with the supporting layer. For a pristine bilayer at normal incidence, the 2nd order diffraction spots should be ca. 3.6x as intense as the monolayer,[23] however, here we observe a 1.9x increase (six-fold symmetry-averaged). Additionally, the 1st order diffraction spot for the bilayer should be the same intensity as the monolayer, and here we observe a 1.4x increase. These observations are consistent with the presence of strain in the bilayer (evident as modulations in the intensity of the bilayer[36] in Figure 4(c)) and/or a variation of surface normal across the field of view. The intensity vs. ϕ plot for region II shows a two-fold increase in the intensity in the peak over region I consistent with the assignment of region II as an aligned bilayer. Region III yields a diffraction pattern that is the superposition of two monolayer diffraction patterns where the second layer is rotated by 28°. Thus, the ϕ-scan DF data can identify and quantify twisted bilayers provided the twist angle is not so small as to cause significant overlap of the diffracted discs.

3. Discussion

We have shown that the ϕ-scan DF technique can sample the diffraction pattern of graphene determining lattice orientation of monolayers and discerning the misorientation of twisted bilayers. For monolayer films the ultimate resolution limitation is the beam spot size, though microscope cleanliness and the buildup of surface contamination due to the electron beam can be problematic at high magnifications. Although the upper limit on the sample area that can be investigated in a single field of view is based on the mixing between real and reciprocal space as the beam scans the sample, tiling can also be used to expand the field of view arbitrarily. In the present case, we demonstrate that orientation mapping on a 53 μm field of view in $<$ 9 minutes collected with an effective pixel data collection rate of 940 pixels/second. An alternative method of performing such an orientation mapping is to use an imaging detector to record diffraction patterns at each sample point,[37] however optically coupled sensors will potentially suffer from lower signal-to-noise, and direct electron sensors are not commercially available for the SEM.[38] The single element diode detector used here is ideal for the ϕ-scan DF technique, but a scintillator/PMT based detector should be viable as well.

For monolayer films, the angular resolution of the orientation map is primarily dominated by the signal to noise of the plot of intensity vs. ϕ and is on the order of 1° for the data in this manuscript. Increasing the sampling of ϕ at the expense of experiment duration should improve this resolution. Alternatively, techniques such as total variation denoising should improve the angular resolution via spatial averaging.[39] For bilayer samples, the diameter of the BF disc will limit the twist angle measurement, and thus using smaller beam convergence angles and a larger sampling of ϕ (i.e. smaller sample rotation increments) should improve the twist angle resolution. Using the width in ϕ of the 2nd order diffraction disc as the ultimate resolution of the twist angle (using deconvolution) yields a 1.8° twist angle resolution for the smallest condenser aperture on this microscope. Modern SEMs with adjustable condenser lenses and multi-lens condenser systems permit significantly more parallel beams and thus higher resolution measurements of the twist angle at the expense of spatial resolution. Alternatively, analyzing moire patterns may be more suitable for measuring very small twist angles.[36]

Herein, the 2nd order diffraction spots were chosen over the 1st order diffraction spots and this deserves some comment. First, we note that the same experiment/analysis could have been performed using a mask that accepted the 1st order diffraction spots instead of the 2nd order diffraction spots, however, the 2nd order spots have several advantages. For monolayer graphene, the 2nd order spots are nearly as intense as the first order spots, while the larger scattering angle gives a lower background from the contribution of non-crystalline scattering (i.e., contamination); thus, overall the signal to noise is improved. Additionally, larger scattering angles permit improved angular resolution of the in-plane angle because while the diffraction spot size is unchanged, the circumference of the annulus that they scatter into is increased. Finally, the 2nd order diffraction spots are significantly more sensitive to the presence of AB-stacked graphene due to the structure factors.[31, 32] It is quite possible that other 2D materials will benefit from a different mask geometry.

A significant benefit to performing these measurements in an SEM is that almost everything is intrinsically computer controlled if permitted by the microscope software. The experiments performed here were fully automated and required no user input during the course of collecting the set of ϕ-scan DF images. Additionally, for microscopes already equipped with even the most rudimentary of transmission detectors, only minimal hardware investment is required – just a mask and sample holder needs to be created. And while the mask used in this work has hexagonal symmetry to match the graphene lattice, a simple circular aperture displaced from the optic axis also works. The main benefits of using a hexagonal aperture are a six-fold increase in signal and a reduced sensitivity to variations in the surface normal of the sample. We note that the imaging transmission detector[27] used to collect the diffraction patterns in this manuscript is not necessary to perform the ϕ-scan DF experiments – these diffraction patterns were only used to clarify what the ϕ-scan DF experiments were sampling.

It is worth mentioning how the ϕ-scan method presented here compares to more established SEM-based elec-

tron diffraction techniques. The most common orientation mapping methods in an SEM – electron backscatter diffraction (EBSD) and electron channeling contrast imaging (ECCI) – use Kikuchi or channeling bands to determine the crystal orientation. The formation of Kikuchi and channeling bands requires a dynamical diffraction model and relies on multiple scattering.[40] In the case of single or few-layer 2D materials at SEM beam energies, multiple scattering is minimal prohibiting the observation of Kikuchi/channeling bands; no data has been published to our knowledge that is inconsistent with this understanding. Therefore, while EBSD or ECCI are expected to be useful for bulk-like samples, they are not expected to be practical techniques for characterizing single or few-layer 2D materials.

Given its low atomic number and single layer thickness, graphene is perhaps the most challenging case for 2D material grain orientation mapping. Therefore, characterizing other two-dimensional materials should also be viable with this technique. Perhaps the most notable limitation of this technique is that it requires an electron transparent (suspended) sample, however, layer transfer techniques are widely known[41, 42] and the success of DF TEM implies that this is not a particularly limiting issue.

4. Conclusions

In conclusion, we have presented the ϕ-scan DF imaging technique for acquiring orientation maps of graphene in an SEM. The technique is fast and should be directly applicable to the vast array of existing and rapidly emerging 2D materials. Our hope is that by enabling DF imaging of 2D materials in an SEM, this technique will allow a significantly broader audience to perform quantitative characterization of grain size and orientation, and thus better understand the effects of grain boundaries on device performance and reliability measurements.

Acknowledgments

We thank Ryan White (NIST) and Ann Chiaramonti Debay (NIST) for helpful microscopy related discussions. This work was performed while B.W.C. held a National Research Council Postdoctoral Associateship.

References

References

[1] S. Z. Butler, S. M. Hollen, L. Cao, Y. Cui, J. A. Gupta, H. R. Gutiérrez, T. F. Heinz, S. S. Hong, J. Huang, A. F. Ismach, E. Johnston-Halperin, M. Kuno, V. V. Plashnitsa, R. D. Robinson, R. S. Ruoff, S. Salahuddin, J. Shan, L. Shi, M. G. Spencer, M. Terrones, W. Windl, J. E. Goldberger, Progress, Challenges, and Opportunities in Two-Dimensional Materials Beyond Graphene, ACS Nano 7 (4) (2013) 2898–2926. doi:10.1021/nn400280c.
URL http://pubs.acs.org/doi/10.1021/nn400280c

[2] A. Bagri, S.-P. Kim, R. S. Ruoff, V. B. Shenoy, Thermal transport across Twin Grain Boundaries in Polycrystalline Graphene from Nonequilibrium Molecular Dynamics Simulations, Nano Lett. 11 (9) (2011) 3917–3921. doi:10.1021/nl202118d.
URL http://pubs.acs.org/doi/abs/10.1021/nl202118d

[3] P. Yasaei, A. Fathizadeh, R. Hantehzadeh, A. K. Majee, A. El-Ghandour, D. Estrada, C. Foster, Z. Aksamija, F. Khalili-Araghi, A. Salehi-Khojin, Bimodal Phonon Scattering in Graphene Grain Boundaries, Nano Lett. 15 (7) (2015) 4532–4540. doi:10.1021/acs.nanolett.5b01100.
URL http://pubs.acs.org/doi/10.1021/acs.nanolett.5b01100

[4] O. V. Yazyev, S. G. Louie, Electronic transport in polycrystalline graphene, Nat. Mater. 9 (10) (2010) 806–809. arXiv:1007.1703, doi:10.1038/nmat2830.
URL http://dx.doi.org/10.1038/nmat2830http://www.nature.com/articles/nmat2830

[5] A. W. Tsen, L. Brown, M. P. Levendorf, F. Ghahari, P. Y. Huang, R. W. Havener, C. S. Ruiz-Vargas, D. A. Muller, P. Kim, J. Park, Tailoring Electrical Transport Across Grain Boundaries in Polycrystalline Graphene, Science 336 (6085) (2012) 1143–1146. doi:10.1126/science.1218948.
URL http://www.sciencemag.org/cgi/doi/10.1126/science.1218948

[6] R. Grantab, V. B. Shenoy, R. S. Ruoff, Anomalous Strength Characteristics of Tilt Grain Boundaries in Graphene, Science 330 (6006) (2010) 946–948. doi:10.1126/science.1196893.
URL http://www.sciencemag.org/cgi/doi/10.1126/science.1196893

[7] H. I. Rasool, C. Ophus, W. S. Klug, A. Zettl, J. K. Gimzewski, Measurement of the intrinsic strength of crystalline and polycrystalline graphene, Nat. Commun. 4 (1) (2013) 2811. doi:10.1038/ncomms3811.
URL http://dx.doi.org/10.1038/ncomms3811http://www.nature.com/articles/ncomms3811

[8] G.-H. Lee, R. C. Cooper, S. J. An, S. Lee, A. van der Zande, N. Petrone, A. G. Hammerberg, C. Lee, B. Crawford, W. Oliver, J. W. Kysar, J. Hone, High-Strength Chemical-Vapor-Deposited Graphene and Grain Boundaries, Science 340 (6136) (2013) 1073–1076. doi:10.1126/science.1235126.
URL http://www.sciencemag.org/cgi/doi/10.1126/science.1235126

[9] Y. Cao, V. Fatemi, S. Fang, K. Watanabe, T. Taniguchi, E. Kaxiras, P. Jarillo-Herrero, Unconventional superconductivity in magic-angle graphene superlattices, Nature 556 (7699) (2018) 43–50. doi:10.1038/nature26160.
URL http://dx.doi.org/10.1038/nature26160http://www.nature.com/doifinder/10.1038/nature26160

[10] D. W. Kim, Y. H. Kim, H. S. Jeong, H.-t. Jung, Direct visualization of large-area graphene domains and boundaries by optical birefringency, Nat. Nanotechnol. 7 (1) (2012) 29–34. doi:10.1038/nnano.2011.198.
URL http://www.nature.com/articles/nnano.2011.198

[11] H. Ago, S. Fukamachi, H. Endo, P. Solís-Fernández, R. Mohamad Yunus, Y. Uchida, V. Panchal, O. Kazakova, M. Tsuji, Visualization of Grain Structure and Boundaries of Polycrystalline Graphene and Two-Dimensional Materials by Epitaxial Growth of Transition Metal Dichalcogenides, ACS Nano 10 (3) (2016) 3233–3240. doi:10.1021/acsnano.5b05879.
URL http://pubs.acs.org/doi/10.1021/acsnano.5b05879

[12] N. Kumar, S. Najmaei, Q. Cui, F. Ceballos, P. M. Ajayan, J. Lou, H. Zhao, Second harmonic microscopy of monolayer MoS2, Phys. Rev. B 87 (16) (2013) 161403. doi:10.1103/PhysRevB.87.161403.
URL https://link.aps.org/doi/10.1103/PhysRevB.87.161403

[13] Y. Li, Y. Rao, K. F. Mak, Y. You, S. Wang, C. R. Dean, T. F. Heinz, Probing Symmetry Properties of Few-Layer MoS 2 and h-BN by Optical Second-Harmonic Generation, Nano Lett. 13 (7) (2013) 3329–3333. doi:10.1021/nl401561r.
URL http://pubs.acs.org/doi/10.1021/nl401561r

[14] S. Hembacher, F. J. Giessibl, J. Mannhart, C. F. Quate, Revealing the hidden atom in graphite by low-temperature atomic force microscopy, Proc. Natl. Acad. Sci. USA 100 (22) (2003) 12539–12542. doi:10.1073/pnas.2134173100.
URL http://www.pnas.org/cgi/doi/10.1073/pnas.2134173100

[15] J. C. Meyer, C. Kisielowski, R. Erni, M. D. Rossell, M. F. Crommie, A. Zettl, Direct Imaging of Lattice Atoms and Topological Defects in Graphene Membranes, Nano Lett. 8 (11) (2008) 3582–3586. doi:10.1021/nl801386m.
URL http://pubs.acs.org/doi/abs/10.1021/nl801386m

[16] M. H. Gass, U. Bangert, A. L. Bleloch, P. Wang, R. R. Nair, A. K. Geim, Free-standing graphene at atomic resolution, Nat. Nanotechnol. 3 (11) (2008) 676–681. doi:10.1038/nnano.2008.280.
URL http://www.nature.com/articles/nnano.2008.280

[17] K. Kim, Z. Lee, W. Regan, C. Kisielowski, M. F. Crommie, A. Zettl, Grain Boundary Mapping in Polycrystalline Graphene, ACS Nano 5 (3) (2011) 2142–2146. doi:10.1021/nn1033423.
URL http://pubs.acs.org/doi/10.1021/nn1033423

[18] P. Y. Huang, C. S. Ruiz-Vargas, A. M. van der Zande, W. S. Whitney, M. P. Levendorf, J. W. Kevek, S. Garg, J. S. Alden, C. J. Hustedt, Y. Zhu, J. Park, P. L. McEuen, D. A. Muller, Grains and grain boundaries in single-layer graphene atomic patchwork quilts, Nature 469 (7330) (2011) 389–392. arXiv:1009.4714, doi:10.1038/nature09718.
URL http://www.nature.com/doifinder/10.1038/nature09718http://www.nature.com/articles/nature09718

[19] J. Kraus, S. Böcklein, R. Reichelt, S. Günther, B. Santos, T. O. Menteş, A. Locatelli, Towards the perfect graphene membrane? – Improvement and limits during formation of high quality graphene grown on Cu-foils, Carbon 64 (2013) 377–390. doi:10.1016/j.carbon.2013.07.090.
URL http://linkinghub.elsevier.com/retrieve/pii/S0008622313007240

[20] W. Zhao, B. Xia, L. Lin, X. Xiao, P. Liu, X. Lin, H. Peng, Y. Zhu, R. Yu, P. Lei, J. Wang, L. Zhang, Y. Xu, M. Zhao, L. Peng, Q. Li, W. Duan, Z. Liu, S. Fan, K. Jiang, Low-energy transmission electron diffraction and imaging of large-area graphene, Sci. Adv. 3 (9) (2017) e1603231. doi:10.1126/sciadv.1603231.
URL http://advances.sciencemag.org/lookup/doi/10.1126/sciadv.1603231

[21] H.-P. Komsa, J. Kotakoski, S. Kurasch, O. Lehtinen, U. Kaiser, A. V. Krasheninnikov, Two-Dimensional Transition Metal Dichalcogenides under Electron Irradiation: Defect Production and Doping, Phys. Rev. Lett. 109 (3) (2012) 035503. arXiv:1206.4407, doi:10.1103/PhysRevLett.109.035503.
URL https://link.aps.org/doi/10.1103/PhysRevLett.109.035503

[22] J. H. Choi, J. Lee, S. M. Moon, Y.-T. Kim, H. Park, C. Y. Lee, A Low-Energy Electron Beam Does Not Damage Single-Walled Carbon Nanotubes and Graphene, J. Phys. Chem. Lett. 7 (22) (2016) 4739–4743. doi:10.1021/acs.jpclett.6b02185.
URL http://pubs.acs.org/doi/abs/10.1021/acs.jpclett.6b02185http://pubs.acs.org/doi/10.1021/acs.jpclett.6b02185

[23] B. Shevitski, M. Mecklenburg, W. A. Hubbard, E. R. White, B. Dawson, M. S. Lodge, M. Ishigami, B. C. Regan, Dark-field transmission electron microscopy and the Debye-Waller factor of graphene, Phys. Rev. B 87 (4) (2013) 045417. doi:10.1103/PhysRevB.87.045417.
URL https://link.aps.org/doi/10.1103/PhysRevB.87.045417

[24] J. Holm, R. R. Keller, Angularly-selective transmission imaging in a scanning electron microscope, Ultramicroscopy 167 (2016) 43–56. doi:10.1016/j.ultramic.2016.05.001.
URL http://linkinghub.elsevier.com/retrieve/pii/S0304399116300559https://linkinghub.elsevier.com/retrieve/pii/S0304399116300559

[25] D. G. Lowe, Distinctive Image Features from Scale-Invariant Keypoints, Int. J. Comput. Vision 60 (2) (2004) 91–110. doi:10.1023/B:VISI.0000029664.99615.94.
URL http://link.springer.com/10.1023/B:VISI.0000029664.99615.94

[26] K. A. Hujsak, B. D. Myers, J. Grovogui, V. P. Dravid, Stage-Rocked Electron Channeling for Crystal Orientation Mapping, Sci. Rep. 8 (1) (2018) 5175. doi:10.1038/s41598-018-23413-3.
URL http://dx.doi.org/10.1038/s41598-018-23413-3http://www.nature.com/articles/s41598-018-23413-3

[27] B. W. Caplins, J. D. Holm, R. R. Keller, Transmission imaging with a programmable detector in a scanning electron microscope, Ultramicroscopy 196 (2019) 40–48. doi:10.1016/j.ultramic.2018.09.006.
URL https://linkinghub.elsevier.com/retrieve/pii/S0304399118301578

[28] W. Zhu, T. Low, V. Perebeinos, A. A. Bol, Y. Zhu, H. Yan, J. Tersoff, P. Avouris, Structure and Electronic Transport in Graphene Wrinkles, Nano Lett. 12 (7) (2012) 3431–3436. doi:10.1021/nl300563h.
URL http://pubs.acs.org/doi/10.1021/nl300563h

[29] K. Kim, Z. Lee, B. D. Malone, K. T. Chan, B. Alemán, W. Regan, W. Gannett, M. F. Crommie, M. L. Cohen, A. Zettl, Multiply folded graphene, Phys. Rev. B 83 (24) (2011) 245433. doi:10.1103/PhysRevB.83.245433.
URL https://link.aps.org/doi/10.1103/PhysRevB.83.245433

[30] Y. Zhou, R. O'Connell, P. Maguire, H. Zhang, High throughput secondary electron imaging of organic residues on a graphene surface, Sci. Rep. 4 (1) (2015) 7032. doi:10.1038/srep07032.
URL http://www.nature.com/srep/2014/141113/srep07032/full/srep07032.htmlhttp://www.nature.com/articles/srep07032

[31] J. Meyer, A. Geim, M. Katsnelson, K. Novoselov, D. Obergfell, S. Roth, C. Girit, A. Zettl, On the roughness of single- and bi-layer graphene membranes, Solid State Commun. 143 (1-2) (2007) 101–109. doi:10.1016/j.ssc.2007.02.047.
URL http://linkinghub.elsevier.com/retrieve/pii/S003810980700316X

[32] J. Ping, M. S. Fuhrer, Layer Number and Stacking Sequence Imaging of Few-Layer Graphene by Transmission Electron Microscopy, Nano Lett. 12 (9) (2012) 4635–4641. doi:10.1021/nl301932v.
URL http://pubs.acs.org/doi/10.1021/nl301932v

[33] K. V. Mardia, P. E. Jupp (Eds.), Directional Statistics, Wiley Series in Probability and Statistics, John Wiley & Sons, Inc., Hoboken, NJ, USA, 1999. doi:10.1002/9780470316979.
URL http://doi.wiley.com/10.1002/9780470316979

[34] S. Yamashita, S. Koshiya, T. Nagai, J. Kikkawa, K. Ishizuka, K. Kimoto, Quantitative annular dark-field imaging of single-layer graphene—II: atomic-resolution image contrast, Microscopy 64 (6) (2015) 409–418. doi:10.1093/jmicro/dfv053.
URL https://academic.oup.com/jmicro/article-lookup/doi/10.1093/jmicro/dfv053

[35] A. R. Gillespie, A. B. Kahle, R. E. Walker, Color enhancement of highly correlated images. I. Decorrelation and HSI contrast stretches, Remote Sens. Environ. 20 (3) (1986) 209–235. doi:10.1016/0034-4257(86)90044-1.
URL http://linkinghub.elsevier.com/retrieve/pii/0034425786900441

[36] L. Brown, R. Hovden, P. Huang, M. Wojcik, D. A. Muller, J. Park, Twinning and Twisting of Tri- and Bilayer Graphene, Nano Lett. 12 (3) (2012) 1609–1615. doi:10.1021/nl204547v.
URL http://pubs.acs.org/doi/10.1021/nl204547v

[37] Y. Han, K. Nguyen, M. Cao, P. Cueva, S. Xie, M. W. Tate, P. Purohit, S. M. Gruner, J. Park, D. A. Muller, Strain Mapping of Two-Dimensional Heterostructures with Sub-picometer Precision, Nano Lett. 18 (6) (2018) 3746–3751. arXiv:1801.08053, doi:10.1021/acs.nanolett.8b00952.
URL http://pubs.acs.org/doi/10.1021/acs.nanolett.8b00952

[38] A. Faruqi, G. McMullan, Direct imaging detectors

for electron microscopy, Nucl. Instrum. Methods Phys. Res. Sect. A 878 (July 2017) (2018) 180–190. doi:10.1016/j.nima.2017.07.037.
URL http://dx.doi.org/10.1016/j.nima.2017.07.037https://linkinghub.elsevier.com/retrieve/pii/S0168900217307787

[39] L. I. Rudin, S. Osher, E. Fatemi, Nonlinear total variation based noise removal algorithms, Phys. D (Amsterdam, Neth.) 60 (1-4) (1992) 259–268. arXiv:arXiv:1011.1669v3, doi:10.1016/0167-2789(92)90242-F.
URL http://linkinghub.elsevier.com/retrieve/pii/016727899290242F

[40] A. Winkelmann, C. Trager-Cowan, F. Sweeney, A. P. Day, P. Parbrook, Many-beam dynamical simulation of electron backscatter diffraction patterns, Ultramicroscopy 107 (4-5) (2007) 414–421. doi:10.1016/j.ultramic.2006.10.006.

[41] J. Kang, D. Shin, S. Bae, B. H. Hong, Graphene transfer: key for applications, Nanoscale 4 (18) (2012) 5527. doi:10.1039/c2nr31317k.
URL http://xlink.rsc.org/?DOI=c2nr31317k

[42] M. Chen, R. C. Haddon, R. Yan, E. Bekyarova, Advances in transferring chemical vapour deposition graphene: a review, Mater. Horiz. 4 (6) (2017) 1054–1063. doi:10.1039/C7MH00485K.
URL http://xlink.rsc.org/?DOI=C7MH00485K